JOURNAL OF GEOPHYSICAL RESEARCH, VOL. 111, D12313, doi:10.1029/2005JD006518, 2006

Influences of man-made emissions and climate changes on tropospheric ozone, methane, and sulfate at 2030 from a broad range of possible futures

Nadine Unger,[1] Drew T. Shindell,[1] Dorothy M. Koch,[1] Markus Amann,[2] Janusz Cofala,[2] and David G. Streets[3]

Received 19 July 2005; revised 18 January 2006; accepted 1 March 2006; published 27 June 2006.

[1] We apply the Goddard Institute for Space Studies composition-climate model to an assessment of tropospheric O_3, CH_4, and sulfate at 2030. We compare four different anthropogenic emissions forecasts: A1B and B1 from the Intergovernmental Panel on Climate Change Special Report on Emissions Scenarios and Current Legislation (CLE) and Maximum Feasible Reduction (MFR) from the International Institute for Applied Systems Analysis. The projections encompass a wide range of possible man-made emissions changes. The A1B, B1, and CLE forecasts all suggest large increases in surface O_3 and sulfate baseline pollution at tropical and subtropical latitudes, especially over the Indian subcontinent, where the pollution increases may be as large as 100%. The ranges of annual mean regional ground level O_3 and sulfate changes across all scenarios are -10 to +30 ppbv and -1200 to +3000 pptv, respectively. Physical climate changes reduce future surface O_3, but tend to increase ground level sulfate locally over North Africa because of an enhancement of aqueous-phase SO_2 oxidation. For all examined future scenarios the combined sum of the CH_4, O_3, and sulfate radiative forcings is positive, even for the MFR scenario, because of the large reduction in sulfate. For A1B the forcings are as much as half of that of the preindustrial to present-day forcing for each species. For MFR the sign of the forcing for each species is reversed with respect to the other scenarios. At 2030, global changes in climate-sensitive natural emissions of CH_4 from wetlands, NO_x from lightning, and dimethyl sulfide from the ocean appear to be small (<5%).

Citation: Unger, N., D. T. Shindell, D. M. Koch, M. Amann, J. Cofala, and D. G. Streets (2006), Influences of man-made emissions and climate changes on tropospheric ozone, methane, and sulfate at 2030 from a broad range of possible futures, *J. Geophys. Res.*, *111*, D12313, doi:10.1029/2005JD006518.

1. Introduction

[2] Two of the major global environmental problems of our time, human-induced climate change and air pollution, are coupled by several trace species in the troposphere including ozone (O_3), methane (CH_4) and sulfate aerosol. CH_4 is emitted directly, but O_3 and sulfate are secondary pollutants formed in the troposphere from the photooxidation of precursor emissions. Human activities and population growth since the preindustrial era have increased emissions of precursor gases and resulted directly in significantly enhanced burdens of O_3, CH_4, and sulfate in the troposphere. Methane is the second most important greenhouse gas forcing with an estimated value of 0.5 Wm^{-2} since the preindustrial [*Ramaswamy et al.*, 2001]. O_3 is a potent greenhouse gas with a direct forcing of $+0.35 \pm 0.15$ Wm^{-2} since the preindustrial [*Ramaswamy et al.*, 2001]. The direct radiative forcing of sulfate may be -0.2 to -0.9 Wm^{-2} since the preindustrial [*Penner et al.*, 2001], the indirect effects (the impact of sulfate aerosols on cloud cover and lifetime) are uncertain but likely to be negative in sign. O_3 pollution has known adverse effects on human health, agriculture and ecosystems (for example, http://www.healtheffects.org and *Emberson et al.* [2003]). Sulfate aerosol is implicated in damage to human health [e.g., *Pope*, 2004] and the environment through acid deposition and visibility reduction. Tropospheric O_3 and sulfate are relatively short-lived (days to weeks) and have heterogeneous spatial distributions. CH_4 has a reasonably long atmospheric lifetime (9–10 years) and a relatively homogeneous tropospheric distribution, thus permitting inclusion in the Kyoto Protocol.

[3] O_3 is formed via the photochemical oxidation of carbon monoxide (CO), methane (CH_4) or non-methane volatile organic compounds (NMVOCs) in the presence of nitrogen oxides (NO_x, $NO_x = NO + NO_2$). Sulfate is formed

[1] NASA Goddard Institute for Space Studies, Columbia University, New York, New York, USA.
[2] International Institute for Applied Systems Analysis, Laxenburg, Austria.
[3] Argonne National Laboratory, Argonne, Illinois, USA.

0148-0227/06/2005JD006518$09.00

in the troposphere from the photooxidation of sulfur dioxide (SO_2) emissions. In the gas phase, the SO_2 oxidation is initiated by the hydroxyl radical (OH) and this process leads to the formation of new sulfate particles. Inside clouds, in preexisting water droplets, SO_2 may be oxidized by dissolved hydrogen peroxide (H_2O_2), a faster process than the gas-phase oxidation.

[4] Fossil fuel combustion processes are the major man-made sources of both O_3 and sulfate precursors. Transportation is a major source of both NO_x and CO emissions, power generation is also important for NO_x emissions while domestic biofuel burning is important for CO emissions. The primary man-made source of SO_2 emissions is the burning of coal and oil for electric power generation. Coal burning accounts for nearly 50% of global SO_2 emissions. SO_2 is also emitted during industrial and manufacturing processes such as metal smelting and pulp and paper manufacturing. The man-made sources of NMVOCs are more diversified than CO and NO_x and include fossil fuel combustion (especially vehicles), industrial chemicals production, oil products handling and solvent evaporation. About 60% of global CH_4 emissions are related to human activities, including fossil fuel production, animal husbandry, rice cultivation, biomass burning, and waste management.

[5] In addition to being coupled through co-location of precursor emissions, strong couplings exist between O_3, sulfate and CH_4 through tropospheric photochemistry. CH_4 oxidation is a major source of background O_3. Meanwhile, O_3 photolysis is the major source of OH, which is the main tropospheric sink for CH_4. The formation rate of sulfate depends critically on the availability of tropospheric oxidants OH and H_2O_2. The formation of H_2O_2 is intimately connected to the presence of OH. Sulfate feeds back on the oxidant chemistry by providing a surface for the heterogeneous conversion of NO_x into nitric acid (HNO_3), which is readily deposited from the system, thereby limiting O_3 production. Hence tropospheric perturbations in either CH_4, O_3, or sulfate have the potential to affect each other. Because of the importance of CH_4 as both a greenhouse gas and a major source of background O_3, man-made CH_4 emissions have been identified as an attractive target for reduction due to the prospective concurrent mitigation of climate forcing and air pollution [*Hansen et al.*, 2000; *Fiore et al.*, 2002; *Shindell et al.*, 2004; *Dentener et al.*, 2004; *Hansen and Sato*, 2004]. In addition, recent work indicates that CH_4 emissions reductions are viable from a cost perspective [*West and Fiore*, 2005]. The development of climate policy for O_3 and sulfate is complicated because the resultant climate forcings are driven by the emissions of precursor gases in a nonlinear way that is dependent on the location of the emissions [*Rypdal et al.*, 2005]. Regional O_3 production responds strongly to NO_x but reducing NO_x is neutral or possibly the wrong direction for climate [*Fuglestvedt et al.*, 1999; *Wild et al.*, 2001; *Shindell et al.*, 2005; *Naik et al.*, 2005]. Reduction of SO_2 emissions leads to less sulfate and improved public health, but incurs a positive forcing.

[6] Since O_3, CH_4, and sulfate play such important roles in determining the quality of our environment, it is instructive to understand how their distributions are likely to change in the near future. In the coming decades, man-made emissions of the precursor gases (NO_x, CO, CH_4, NMVOCs, and SO_2) are expected to change as more nations industrialize, other nations implement emissions control strategies, and world population grows. The changes in man-made emissions will alter the distributions of O_3, CH_4, and sulfate in the troposphere. At the same time, changes in climate variables, such as temperature, humidity, precipitation, clouds, climate-sensitive natural emissions, circulation and convection, will also affect the tropospheric distributions and lifetimes of O_3, CH_4, and sulfate. For example, *Feichter et al.* [2004] found that the sulfate aerosol load is considerably reduced in a warmer climate relative to the present-day for the same SO_2 source strength because of feedbacks between temperature changes and the hydrological cycle leading to increased wet removal of sulfate. Similarly, O_3 concentrations have been found to decrease in a warmer, wetter climate predominantly because of increased water vapor, which is a chemical sink for O_3 but source of OH [*Stevenson et al.*, 2000; *Johnson et al.*, 2001; *Stevenson et al.*, 2005]. The increased OH concentrations and temperature both contribute to a faster CH_4 oxidation rate in a future warmer climate.

[7] We investigate how the tropospheric distributions of O_3, CH_4, and sulfate will change because of changes in man-made emissions and physical climate changes at 2030. Future changes in human activities are difficult to predict, therefore we explore four different man-made emissions scenarios that encompass a wide range of potential changes in activity. We employ the A1B and B1 storylines from the Intergovernmental Panel on Climate Change (IPCC) Special Report on Emissions Scenarios (SRES) [*Nakicenovic et al.*, 2000] and the Current Legislation (CLE) and Maximum Feasible Reduction (MFR) scenarios developed at the International Institute for Applied Systems Analysis (IIASA) [*Amann et al.*, 1999; *Dentener et al.*, 2004]. The CLE and MFR forecasts have recently been used in multi-model assessments of changes to O_3 radiative forcing [*Stevenson et al.*, 2006]. We improve and extend these previous studies of changes to tropospheric composition at 2030 in several ways: (1) use a broad set of future man-made emissions scenarios, (2) examine the relative influences of man-made emissions changes and physical climate changes, and (3) simulate changes to O_3, CH_4, and sulfate aerosol simultaneously in a fully coupled atmospheric composition-climate model.

[8] The Goddard Institute for Space Studies (GISS) composition-climate model is described in section 2. Our experimental setup is presented in section 3 with descriptions of the man-made emissions scenarios (section 3.1), natural emissions included in the current study (section 3.2) and the set of simulations (section 3.3). In section 4 the results of changes at 2030 relative to the present-day are presented, including climate-sensitive natural emissions (section 4.1), surface O_3 and sulfate air pollution (section 4.2) and O_3, sulfate and CH_4 global budgets (section 4.3). The radiative forcing consequences of each future scenario are presented in section 5. Conclusions are presented in section 6.

2. Model Description

[9] We employ the Goddard Institute for Space Studies (GISS) general circulation model (GCM) version model III

Table 1. Total Anthropogenic and Biomass Burning Trace Gas Emissions Inventories for the Control Simulations and Future Projections[a]

	CO, Tg CO/yr	NO_x, Tg N/yr	NMVOC, Tg C/yr	CH_4, Tg CH_4/yr	SO_2, Tg SO_2/yr
CONT1					
TA	531.0	29.0	112.3	289.4	143.9
BB	314.9	4.2	20.4	13.2	2.6
A1B					
TA	665.0	52.5	184.4	513.2	192.0
BB	344.3	3.9	22.8	20.3	2.8
B1					
TA	463.4	28.5	127.2	409.7	114.2
BB	237.3	3.0	15.1	17.9	1.9
CONT2					
TA	470.0	27.8	96.1	300.6	108.3
BB	507.0	10.2	25.9	23.6	2.8
CLE					
TA	397.1	32.8	94.7	428.8	114.6
BB	507.0	10.2	25.9	23.6	2.8
MFR					
TA	221.7	13.1	60.7	290.0	35.8
BB	507.0	10.2	25.9	23.6	2.8

[a]Total anthropogenic (TA) emissions include fossil fuel, industrial, biofuel, and waste sources. CONT1 and CONT2 are the control simulations, and A1B, B1, CLE, and MFR are the future projections. BB, biomass burning.

with fully interactive tropospheric chemistry and sulfate aerosol modules. Model III is a new reprogrammed and documented version of the GISS GCM, which includes improved representations of several physical processes and produces better climate simulations than any prior GISS GCM based on comparison with a wide suite of observations [*Schmidt et al.*, 2006]. We use 23 vertical layers (model top in the mesosphere at 0.01 mb) and $4^\circ \times 5^\circ$ horizontal resolution.

[10] The tropospheric chemistry and sulfate aerosol modules have been described in detail and evaluated elsewhere [*Shindell et al.*, 2003; *Koch et al.*, 2006]. The tropospheric gas-phase mechanism represents background HO_x-NO_x-O_x-CO-CH_4 chemistry as well as peroxyacetylnitrates, hydrocarbon families, and isoprene based on 32 species and 77 reactions. The sulfate module includes gas-phase and in-cloud formation of sulfate aerosol [*Koch et al.*, 1999]. In the present study, the tropospheric chemistry and sulfate aerosol modules are coupled such that instantaneous oxidant concentrations (OH, NO_3 and H_2O_2) are available to the sulfate module and instantaneous sulfate aerosol mass (SO_4) and sulfur species concentrations (SO_2 and dimethyl sulfide (DMS)) are available to the chemistry module yielding a total of 19 transported tracers (15 from the tropospheric chemistry and four sulfur species) [*Bell et al.*, 2005]. The two-way coupling allows assessment of future feedbacks (either climate or emissions-driven) between the oxidant and sulfate cycles.

[11] Chemical calculations are performed only in the troposphere in the present version of the model. We use a thermal tropopause defined by the meteorological lapse rate. Stratospheric values of O_3, NO_x, and CH_4 are prescribed according to satellite observations with seasonally varying abundances [*Shindell et al.*, 2003].

[12] Our present focus is to quantify the response of the O_3, CH_4, and sulfate tropospheric composition to global changes including emissions and climate. We do not feed back the model generated O_3, CH_4, and sulfate aerosol to the radiation scheme and therefore do not quantify the feedback of the tropospheric chemical changes on the climate system, although we do provide a measure of the climate impacts using the concept of radiative forcing, which has been found to be a robust and useful metric of the potential climatic impact of trace species [*Fuglestvedt et al.*, 2003].

3. Experimental Setup

3.1. Man-Made Emissions

[13] We compare four different future man-made trace gas emissions scenarios. A1B and B1 are based on the IPCC SRES reference models [*Nakicenovic et al.*, 2000] and were generated using regional growth factors for each emission source from the IMAGE socioeconomic model [*IMAGE Team*, 2001]. The CLE and MFR scenarios were developed at IIASA more recently than the IPCC projections using the global version of the Regional Air Pollution Information and Simulation (RAINS) model [*Amann et al.*, 1999]. Further details of the RAINS model and IIASA emissions projections are available at http://www.iiasa.ac.at/rains/global_emiss/global_emiss.html and presented by *Dentener et al.* [2004]. A1B and B1 are from the IPCC storylines that emphasize future sustainable development. The A1B scenario features rapid economic growth with a balance between fossil fuel intensive and renewable energy sources whereas the more optimistic B1 scenario envisages the use of clean and resource efficient technologies. The CLE scenario is based on present emissions control legislation and national expectations of economic growth and takes into account air quality management legislation that was initiated in Asia and Latin America after the IPCC storylines were constructed. The MFR scenario is an optimistic future vision based on world-wide implementation of the available advanced emissions control technologies for trace gases.

[14] Two present-day control trace gas emissions inventories are used in the study. CONT1, for comparison with the IPCC projections (A1B and B1), is based on anthropogenic emissions for 1995 from the Emissions Database for Global Atmospheric Research (EDGAR3.2) representative of the year 1995 [*Olivier and Berdowski*, 2001]. CONT2, for comparison with the IIASA projections, is based on the present-day Current Legislation emissions inventory [*Dentener et al.*, 2004].

[15] The global annual total man-made trace gas emissions for each run (present-day controls and future scenarios) are given in Table 1. The IPCC A1B and B1 projections include changes to biomass burning emissions as described by *Streets et al.* [2004]. The CLE and MFR scenarios use biomass burning emissions from the Global Fire Emissions Data Set (G. V. D. Werf, personal communication, 2005) fixed to present-day values. In addition to the surface sources, the model includes aircraft emissions of NO_x (0.6 Tg N/yr) and SO_2 (0.1 Tg SO_2/yr) [*Baughcum et al.*, 1996]. Since none of the scenarios provide aircraft emissions changes at 2030, we estimate future values by applying a 2.3 growth factor to each projection [*Henderson and Wickrama*, 1999].

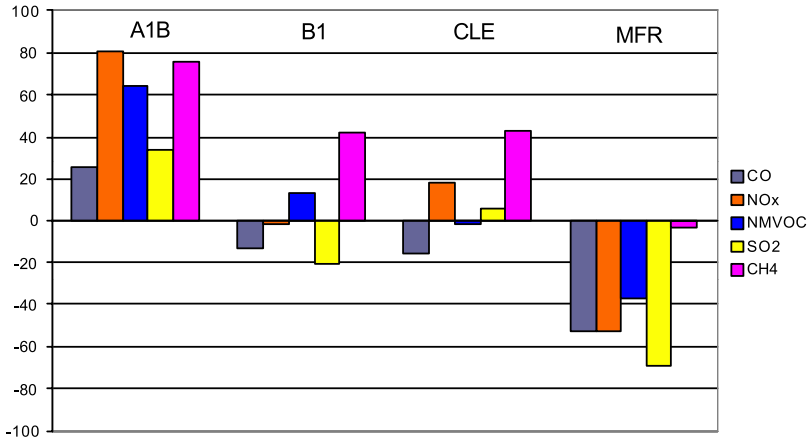

Figure 1. Percentage change in total anthropogenic precursor emissions: CO, NO_x, NMVOCs, CH_4, and SO_2 at 2030 for each scenario relative to the present-day control simulations (CONT1 for A1B and B1; CONT2 for CLE and MFR).

[16] The emissions scenarios encompass a broad range of potential future changes and each has a unique character. The percentage change in total annual global anthropogenic emissions of key trace gases, relative to present-day control (CONT1 for A1B and B1 or CONT2 for CLE and MFR), is given in Figure 1. A1B projects significant global increases in all trace gas emissions while MFR projects significant global decreases in all trace gas emissions. The CH_4 emissions reduction looks somewhat meager for the MFR scenario (about 5%), but should be compared to the CLE CH_4 emission change at 2030. CLE and B1 are generally intermediate between A1B and MFR. CLE and B1 predict similar magnitude global changes in the CO and CH_4 emissions, both scenarios suggest $\sim -15\%$ decrease in CO emissions and a +40% increase in CH_4 emissions. There are significant differences in the NO_x and SO_2 emissions changes between CLE and B1. CLE predicts an increase of +18% in NO_x emissions compared to -2% decrease in the B1 scenario. SO_2 emissions increase by +5% in CLE but decrease by -20% in B1.

[17] In addition to changes in the magnitude of the short-lived precursor emissions (NO_x, CO, NMVOCs, SO_2), changes in the geographical location of the emissions may impact future air pollution and radiative forcing. For example, the resultant climate impacts of a sustained NO_x perturbation through O_3 and CH_4 changes have been found to be different for a perturbation localized in the southeast Asia versus Europe [*Berntsen et al.*, 2005]. In the case of sulfate aerosol, an equal reduction in SO_2 emissions has a larger effect on concentrations in Europe compared to China because of different regional rates of oxidation and removal [*Berglen et al.*, 2004]. In the present study, the A1B, B1, and CLE futures all envisage a regional shift in precursor emissions by 2030 with decreases at NH midlatitudes and increases at the more photochemically active subtropical and tropical latitudes. Over the United States and Europe, SO_2 emissions decrease by up to -80% in A1B and B1 and -20% in CLE. Large increases in SO_2 emissions occur over India: 400% in A1B and $\sim$100% in B1 and CLE. CLE has almost no change in SO_2 emissions over China, while B1 has decreases (-30%) and A1B has increases (20%). B1 has the largest decreases in NO_x emissions at the NH midlatitudes (-60% over Europe and the United States). A1B predicts NO_x emissions decreases of -30% over the United States and western Europe, but increases in eastern Europe ($\sim$100%). Fossil fuel NO_x emissions increase by 500% over India in A1B and about 100% in B1 and CLE. B1 has almost no change in NO_x emissions over China in contrast to the increases in A1B (+100%) and CLE (+30%). The precursor emissions changes in MFR are more regionally homogeneous with decreases in SO_2 emissions up to $-80-90\%$ and decreases in NO_x emissions up to -50%.

3.2. Natural Emissions

[18] The model includes additional trace gas emissions from natural sources detailed in Table 2. CH_4 emissions from wetlands are the largest single source to the atmosphere representing about 20–45% of the total emission [e.g., *Hein et al.*, 1997; *Houweling et al.*, 1999; *Matthews*, 2000]. We include climate-sensitive CH_4 emissions from wetlands using a linear parameterization that was derived from a detailed process model such that the emissions are dependent on the climate model's soil temperature and precipitation anomalies [*Shindell et al.*, 2004]. We do not allow the geographic distribution of wetlands to respond to climate for this study. Emissions of NO_x from lightning are climate-sensitive and dependent on the model's convection scheme [*Price et al.*, 1997]. DMS emissions from the oceans are interactive with the model's surface wind speed [*Koch et al.*, 2006]. In the present model formulation, climatological monthly mean emissions of isoprene from vegetation are used from the GEIA data set [*Guenther et al.*, 1995].

3.3. Simulations

[19] A description of the simulations is given in Table 3. Two simulations are performed for each future man-made emissions scenario: (1) with a present-day climate representative of the 1990s (the simulations are annotated with "(e)" to signify emissions changes only) and (2) with a future 2030s climate (the simulations are annotated with "(e+c)" to signify emissions and climate changes), yielding

Table 2. Summary of Natural Trace Gas Emissions in the Present Study

Species	Emission Source	Present-Day Annual Total
CH_4	wetlands and tundra	247 Tg CH_4/yr
CH_4	termites	20 Tg CH_4/yr
CH_4	ocean	13 Tg CH_4/yr
CH_4	lake	6 Tg CH_4/yr
CH_4	ground	7 Tg CH_4/yr
NO_x	soils	5.83 Tg N/yr
NO_x	lightning	6.36 Tg N/yr
Isoprene	vegetation	550 Tg C/yr
NMVOC	vegetation	30 Tg C/yr
SO_2	volcano	10.5 Tg S/yr
DMS	ocean	21.2 Tg S/yr

a total of eight future projections. The present-day control simulations (CONT1 and CONT2) are run with the 1990s climate.

[20] Prescribed decadal average (1990–1999 and 2030–2039) sea surface temperatures and sea ice that were generated in a previous simulation of the GISS atmosphere-ocean model (AOM) [*Russell et al.*, 2000] provide the lower boundary conditions over the oceans. The AOM predictions of Northern Hemisphere regional climate trends show good agreement and high positive spatial correlation with NCEP (National Centers for Environmental Prediction) reanalysis data for 1960 to 2000 [*Lucarini and Russell*, 2002] implying that the model may be reliable in forecasting future climate change. For this study we select data from an AOM simulation that used observed greenhouse gases until 1990 and compounded 0.5% annual increases of CO_2 after 1990. At this rate, CO_2 abundance changes from 360 ppmv at 1995 to 429 ppmv at 2030. To be consistent, the forecast of future climate should be based on the greenhouse gas projections associated with each individual scenario. However, no data are available for CLE and MFR. The CO_2 abundance increases to 454 ppmv and 437 ppmv for the A1B and B1 scenarios respectively [*Intergovernmental Panel on Climate Change*, 2001]. Hence the climate change scenario that we employ represents about three fourths of the climate change from A1B and is about the same as B1. In view of other uncertainties and climatic inertia, the use of the GISS AOM simulation provides a realistic, appropriate "middle-of-the-road" representation of potential future climate change and suits our present purposes in evaluating the relative roles of physical climate changes and anthropogenic emissions changes on tropospheric composition.

[21] The climate change forecast that we employ predicts a global annual mean surface air temperature increase of 0.68°C by the 2030s (Figure 2). Largest Northern Hemisphere warming of up to +2–3°C occurs in Central Asia, North America, and the Barents Sea regions. Over most other continental land areas, the temperature increase is in the range 0.3–1°C. Cooling of about −0.5°C occurs in the high-latitude North Atlantic Ocean and Bering Sea regions. Relative to the Northern Hemisphere, large surface warming occurs over the Antarctic region. As observed in similar models, the AOM simulation that provided the sea surface temperature and sea ice boundary conditions showed poor correlations with NCEP reanalysis data in the Southern Hemisphere, due in part to the model's unrealistic interannual variability in southern sea ice cover [*Russell et al.*, 2000]. Changes in precipitation impact tropospheric chemistry through wet processing. Annual mean precipitation increases by a global average of 0.06 mm/day (∼2%), but there are considerable regional differences (Figure 2). Largest increases in precipitation occur in the tropical Atlantic and western Indian Ocean (1.5–2.5 mm/day, ∼10–20%). Largest decreases occur over the Indian subcontinent, Arabian Sea and Bay of Bengal (1–2 mm/day, ∼10–20%). The temperature increases extend throughout the troposphere (Figure 3) with largest warming in the SH and upper tropical troposphere for this particular model. The lower stratosphere shows some cooling. As a result of the warmer temperatures, zonal mean water vapor mixing ratios increase at 2030 throughout the troposphere by 5–10%. The largest absolute increases are in the tropics and subtropics.

[22] The IPCC simulations (A1B, B1) include a full calculation of CH_4. First, the present-day CH_4 budget source and sink terms were balanced (assuming a growth rate of +14 Tg/yr [*Prather and Ehhalt*, 2001]) by adjusting the stratospheric exchange term. For the future emissions scenarios, an initial CH_4 concentration was estimated according to the emissions increase and then the initial CH_4 trend was extrapolated exponentially using the model's CH_4 adjustment time (12.6 years) to infer the actual CH_4 concentration change at 2030 [*Shindell et al.*, 2005]. How-

Table 3. Description of Simulations

Scenario Family, S	Simulation Name	Emissions	Emissions Year	Climate-Meteorology	Methane
Control IPCC	CONT1	Edgar3.2	1995	1990s	calculated
A1B	A1B(e)	IPCC A1B	2030	1990s	calculated
A1B	A1B(e+c)	IPCC A1B	2030	2030s	calculated
A1B	A1B_CH_4	IPCC A1B	2030	2030s	prescribed to present-day values from CONT1
B1	B1(e)	IPCC B1	2030	1990s	calculated
B1	B1(e+c)	IPCC B1	2030	2030s	calculated
Control IIASA	CONT2	IIASA CLE	2000	1990s	prescribed
CLE	CLE(e)	IIASA CLE	2030	1990s	prescribed
CLE	CLE(e+c)	IIASA CLE	2030	2030s	prescribed
MFR	MFR(e)	IIASA MFR	2030	1990s	prescribed
MFR	MFR(e+c)	IIASA MFR	2030	2030s	prescribed

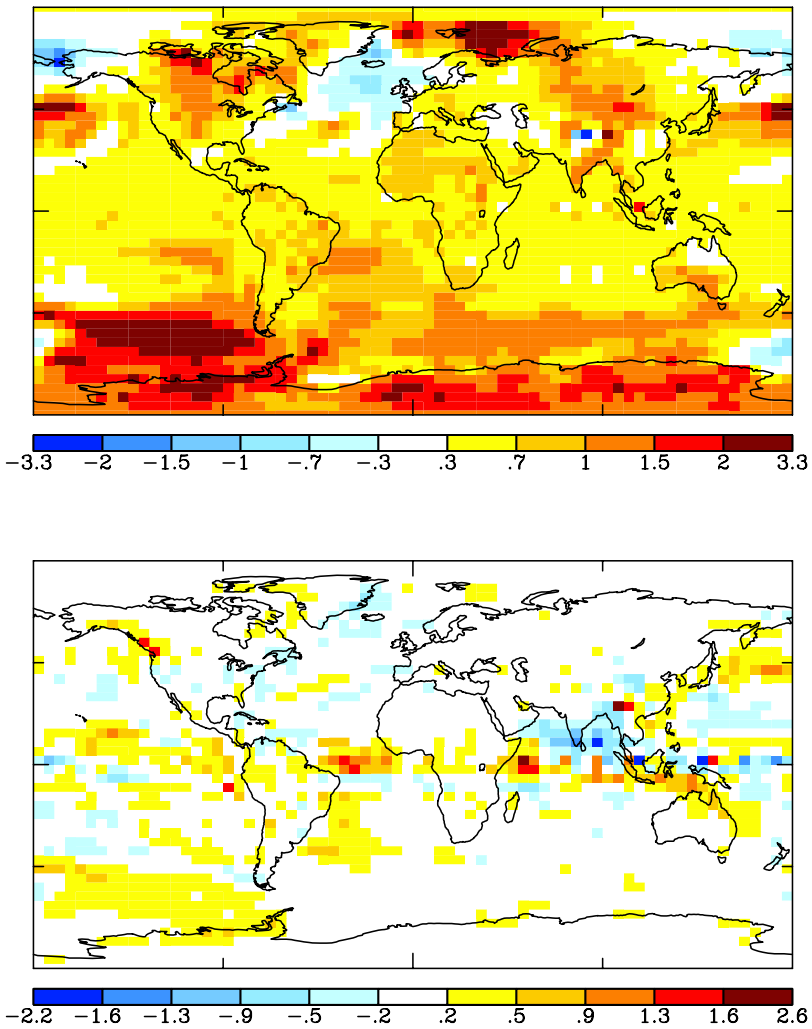

Figure 2. Difference in annual mean (top) surface air temperature (degrees C) and (bottom) precipitation (mm/day), between the 2030s and 1990s climates.

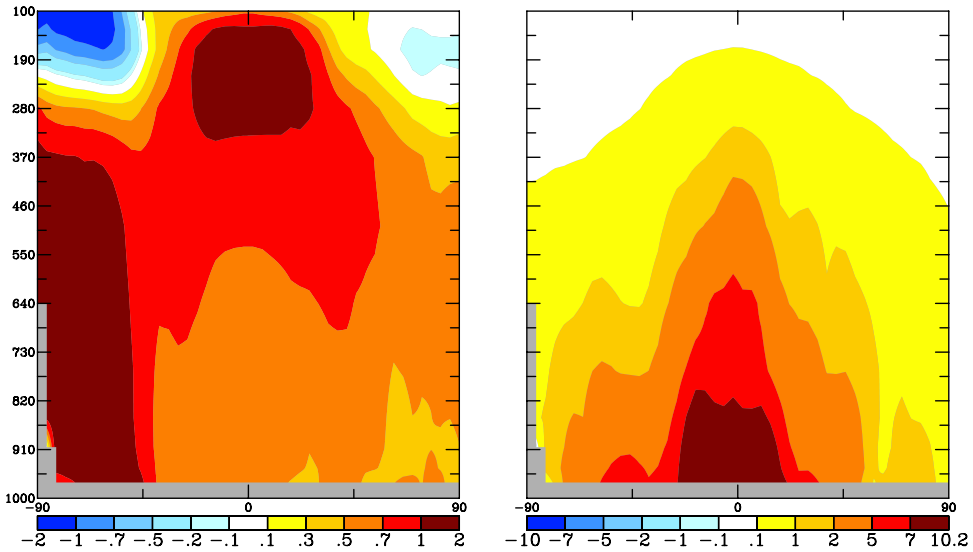

Figure 3. Difference in annual zonal mean (left) temperature (degrees C) and (right) specific humidity (10^2 ppmv), between the 2030s and 1990s climates.

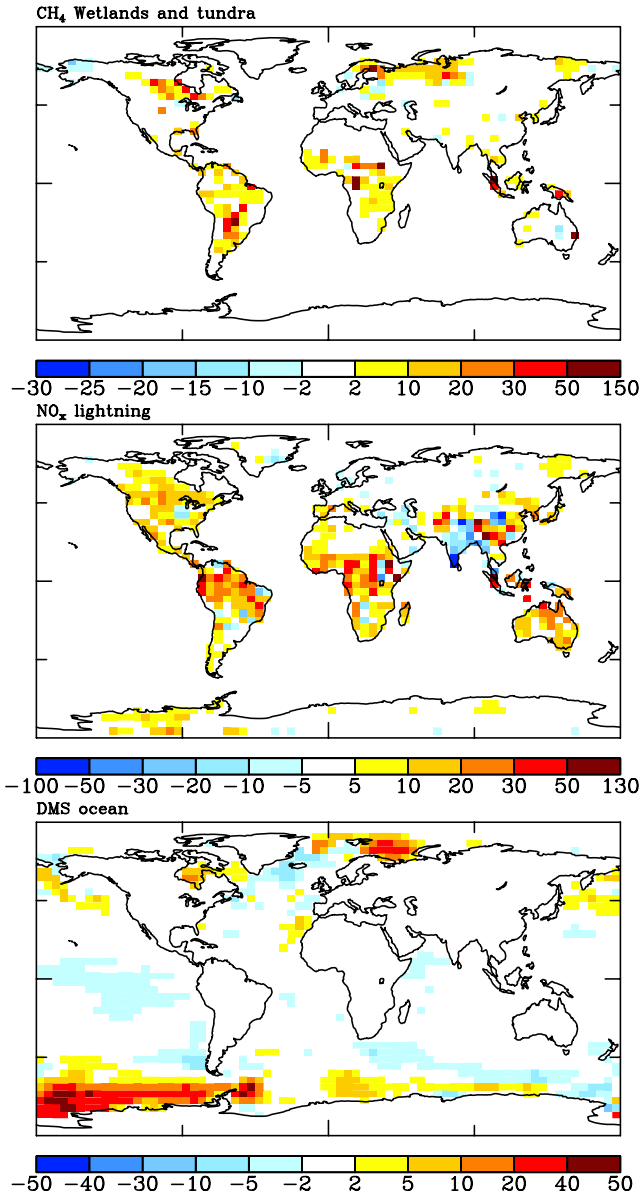

Figure 4. Simulated changes in climate-sensitive natural trace gas emissions between 2030 and the present-day: (top) CH_4 from wetlands and tundra (10^{-12} kg m^{-2} s^{-1}), (middle) NO_x from lightning (10^{-14} kg m^{-2} s^{-1}), and (bottom) DMS from the ocean (10^{-13} kg m^{-2} s^{-1}).

ever, for the IIASA simulations (CLE and MFR), CH_4 concentration is prescribed according to values generated in previous transient simulations using the STOCHEM model [*Dentener et al.*, 2004]. An additional sensitivity simulation is performed (A1B_CH_4) based on A1B(e+c), but with CH_4 concentrations fixed to present-day values taken from CONT1.

[23] The A1B and B1 family simulations were run for 15 years. The first 5 years of the simulation are discarded as spin-up and the remaining 10 are averaged for analysis. The MFR and CLE family simulations were run for 12 years and the first 2 years are discarded as spin-up with the remaining 10 years averaged for analysis. We use 10-year averages to reduce interference from natural interannual climatic variability with the perturbation signal.

4. Results

[24] The difference in a specific diagnostic variable (for example, O_3 mixing ratio) between 2030 and the present-day is calculated for each projection within a scenario family, S, using the appropriate present-day control simulation, C. We derive the emissions-only impacts using the difference between simulations S(e) − C, the climate-only impacts using S(e+c) − S(e) and the combined emissions and climate change impacts using S(e+c) − C. Percentage changes are calculated relative to the appropriate present-day control simulation. Hence the climate-only impacts are determined as the difference between the combined emissions and climate change simulation and the emissions-only simulation and are therefore based on a 2030 background emissions state. Differences between CONT1 and CONT2 are relatively small compared to differences between the future projections and the appropriate present-day control simulation.

4.1. Changes in Climate-Sensitive Natural Emissions at 2030

[25] Physical climate changes drive changes to natural emissions (Figure 4). The climate-sensitive trace gas global total emissions included in this study increase in response to the temperature increase at 2030. Global annual mean CH_4 emissions from wetlands and tundra increase by +16 Tg CH_4/yr from 247 to 263 Tg CH_4/yr at 2030 (∼5%). A projection based on doubled CO_2 (representative of 2100 conditions), using the same emission algorithm, gave an increase in the CH_4 wetlands emissions of +78% for a global mean annual average surface temperature increase of 3.4°C [*Shindell et al.*, 2004]. NO_x generated from lightning increases by 0.3 Tg N/yr from 6.2 to 6.5 Tg N/yr in the present study. *Stevenson et al.* [2005], using a similar formulation in a different GCM, found no trend in NO_x from lightning between the 1990s and 2020s, however they did find important spatial changes. Oceanic DMS emissions increase modestly from 40.9 to 41.3 Tg S/yr with the majority of the increase localized in the western Southern Ocean at high latitudes. Our present study does not include climate-driven changes to isoprene emissions from vegetation. *Stevenson et al.* [2005] found a global increase of 9% in isoprene emissions by 2020 due to increased surface temperatures with most of the increase localized over South America. On short-term future timescales, it seems likely that the most significant changes to isoprene emissions will be a result of land-use changes rather than physical climatic factors.

4.2. Surface Pollution at 2030

[26] O_3 and sulfate pollution levels at a particular location are determined by three factors: (1) the local precursor emissions and meteorology, (2) the synoptic or regional-scale meteorological conditions, and (3) the baseline levels of O_3 and sulfate and their precursors present in ambient air, which depend on large-scale processes such as intercontinental transport of pollutants and precursors [e.g., *Wild and Akimoto*, 2001; *Park et al.*, 2004]. Our global-scale model

Table 4. Relative Roles of Emissions and Climate Changes on the Global Annual Mean Surface O_3 Change at 2030 Relative to the Present-Day[a]

Emissions Family	Emissions-Only Response	Climate-Only Response	Total of Emissions and Climate Response
A1B	4.66	−0.81	3.85
B1	1.17	−0.70	0.47
CLE	1.42	−0.88	0.54
MFR	−1.65	−0.81	−2.46

[a]Units are ppbv.

predictions represent the baseline levels of O_3 and sulfate pollution upon which regional and urban pollution builds and is ideally suited to capturing large-scale influences on O_3 and sulfate. Therefore the changes at 2030 that we forecast are to be considered in the context of changing baseline levels.

4.2.1. Surface Ozone

[27] The change in annual global mean surface O_3 predicted for each scenario is shown in Table 4. The emissions-only changes in CLE and MFR agree well with results from similar experiments in a multimodel study using 25 different models (+1.7 ± 0.3 ppbv for CLE; −1.8 ± 0.5 ppbv for MFR) [*Dentener et al.*, 2006]. Climate changes reduce global mean surface O_3 for all scenarios. In the case of CLE and B1, the climate change response represents about 60% of the emissions change. Indeed, in remote regions over the oceans, climate changes dominate the total change in CLE, B1 and MFR scenarios. The spatial distribution of the climate change-only impacts on surface O_3 is shown in Figure 5 for the B1 scenario (a similar pattern occurs for the other scenarios). Generally, the O_3 reduction is about −1 to −1.5 ppbv but reaches −4 ppbv over the North Atlantic Ocean. Both the production and loss rates of O_3 are changed in a warmer, wetter climate. Increased water vapor increases the rate of reaction of O^1D with water vapor, an effective loss for O_3 (but source for OH). Increased temperatures increase the rate of the photochemical production and loss reactions. In our analysis, the water vapor effect and subsequent O_3 loss appears to dominate in most regions, except India and the north Pacific, resulting in reduced O_3 concentrations due to climate change. The dominant reduction in O_3 mixing ratio due to future physical climate change has been observed in several other studies [*Stevenson et al.*, 2000, 2005; *Johnson et al.*, 2001].

[28] Figure 6 shows the annual mean surface ozone change, including the impacts from emissions and climate changes, for each scenario relative to the control. Consistent across each scenario is that the largest absolute changes occur in subtropical and tropical regions. The surface O_3 changes range from −10 to +30 ppbv depending on the scenario. Maximum surface O_3 increases are forecast over India by three of the scenarios (AlB, B1, and CLE) because of the large regional increases in NO_x precursor emissions there. The largest absolute increases occur for the A1B scenario, which predicts surface O_3 increases everywhere, except for a small decrease in southwest Africa due to a reduction in biomass burning there. In A1B, surface O_3 increases by 25–30 ppbv (60–80%) over the Indian subcontinent and by 10–15 ppbv (30–40%) over North Africa, Central America, the Middle East, and East Asia. A1B forecasts smaller increases of 2–5 ppbv (5–10%) over Europe and the United States, despite reductions in NO_x and CO precursor emissions in those regions. The increases in surface O_3 at NH midlatitudes in A1B appear to be driven by the global increase in CH_4 emissions. Figure 7 shows the impact of holding CH_4 to present-day levels on the A1B(e+c) simulation surface O_3 forecast (A1B_CH_4 – CONT1). Surface O_3 is reduced everywhere relative to the A1B(e+c) forecast (global mean change is reduced to +1.77 ppbv compared to 3.85 ppbv). Hence future global CH_4 emissions increases in an A1B world make a significant contribution to the surface O_3 change at NH midlatitudes and remote regions and potentially compromise the effectiveness of NO_x and CO precursor reductions in those regions. The MFR scenario predicts decreased surface O_3 everywhere with a spatial pattern that mirrors in reverse the A1B scenario (Figure 6). The largest decreases of about 7–10 ppbv (20%) occur across Central America, Asia, and North Africa. Smaller decreases in surface O_3 of about 1–2 ppbv (5%) occur over Northern Hemisphere high-latitude regions. Both the B1 and CLE scenarios predict maximum

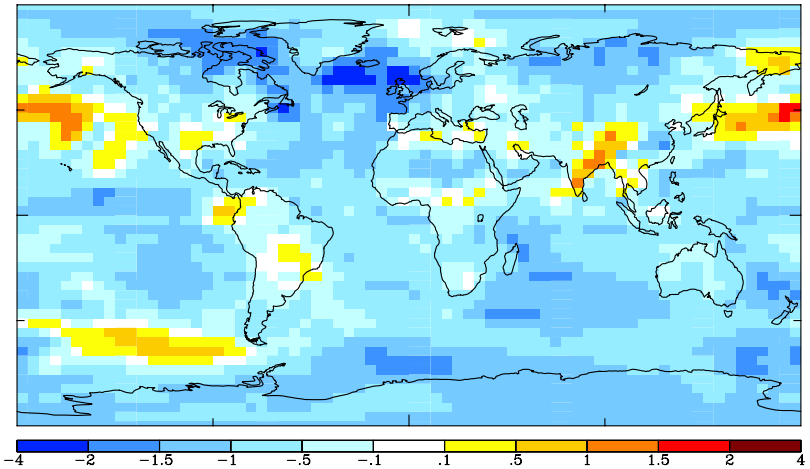

Figure 5. Impact of physical climate changes on surface O_3 (ppbv) at 2030 relative to the present-day calculated using the B1 scenario family.

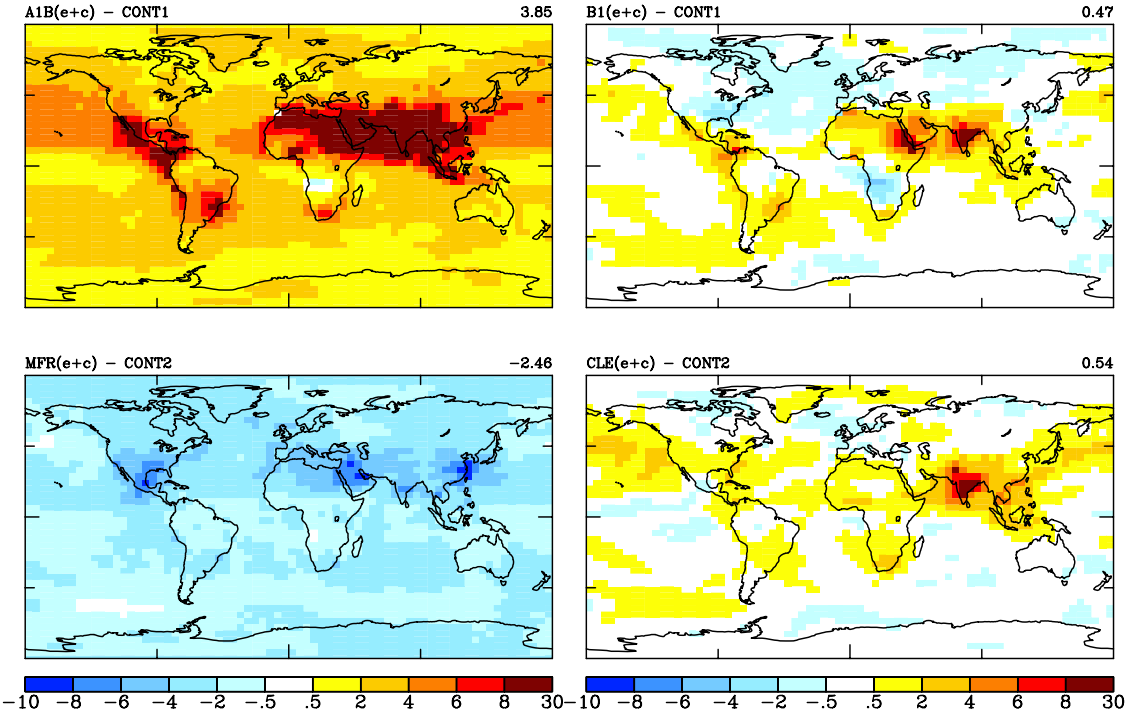

Figure 6. Total change (emissions and climate) in surface O_3 (ppbv) for each scenario family at 2030 relative to the present-day.

surface O_3 increases across the Indian subcontinent of ~10 ppbv (30–40%). B1 has similar increases (5–10ppbv, ~30%) over East Africa and the Middle East, not forecast by the CLE. CLE has increases over Southeast Asia (10%), not present in B1. Both scenarios forecast negligible changes over Europe (< 1ppbv). A difference occurs over the eastern United States, where B1 indicates surface O_3 decreases of up to 4–5ppbv (5–10%) compared to increases of 1–2 ppbv (<5%) in CLE. This difference reflects the different predictions of NO_x emissions over the United States: B1 anticipates reductions of up to −60% whereas CLE envisages increases of around 10%. B1 predicts decreases in surface O_3 over South West Africa due to the reduction in biomass burning whereas CLE did not include future changes to biomass burning emissions.

[29] The surface O_3 increases at 2030 in the subtropical and tropical regions, (India, Africa, Central America, and South East Asia) do not have a strong seasonal cycle (not shown), which is different from the preindustrial to present-day O_3 change predominantly at Northern Hemisphere midlatitudes, which demonstrates a significant seasonality. Plentiful sunlight is always available at the lower latitudes to drive the photochemistry, whereas at higher latitudes the photochemistry is limited by the availability of sunlight. Hence future increases in O_3 air pollution at lower latitudes

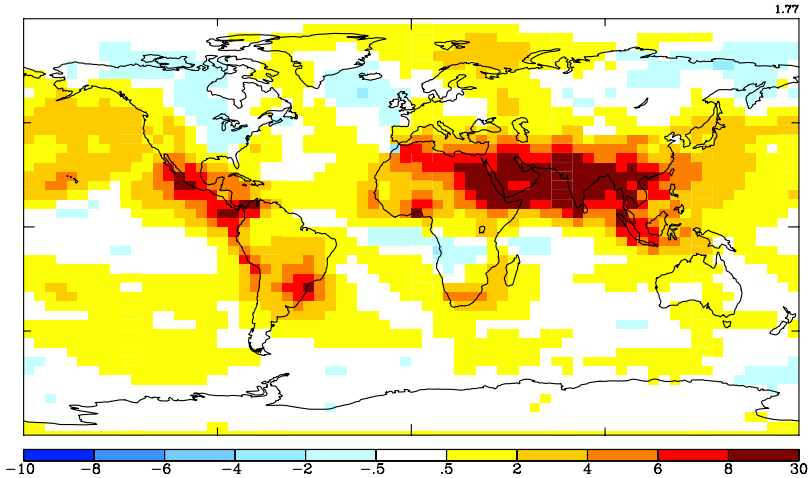

Figure 7. Change in surface O_3 (ppbv) for sensitivity simulation A1B_CH_4 (based on A1B(e+c) with CH_4 held to present-day concentrations) relative to the present-day.

Table 5. Relative Roles of Emissions and Climate Changes on the Global Annual Mean Surface Sulfate Change at 2030 Relative to the Present-Day[a]

Emissions Family	Emissions-Only Response	Climate-Only Response	Total of Emissions and Climate Response
A1B	64.72	4.30	69.02
B1	3.39	2.93	6.32
CLE	3.83	1.55	5.38
MFR	−54.28	0.62	−53.7

[a]Units are pptv.

persist throughout the year in contrast to O_3 pollution at midlatitudes, which is a summertime phenomenon.

4.2.2. Surface Sulfate

[30] On a global scale, the largest annual mean surface sulfate increase occurs for the A1B scenario (+69 pptv) (Table 5). MFR predicts a similar magnitude change but in the opposite direction (−53 pptv). Climate changes cause an increase in surface sulfate for all scenarios. The climate change impact is small compared to the emissions changes for A1B and MFR, but, at least in a global context, appears significant compared to the B1 and CLE emissions changes. The annual mean surface sulfate changes for B1 and CLE are small (+5–6pptv). However, the small global changes belie large regional differences. Indeed, the global changes for A1B, CLE and B1 represent the difference between large decreases at NH midlatitudes and large increases at lower subtropical latitudes, a marked regional redistribution masked by the global change values.

[31] The change in surface sulfate due to climate is localized over North Africa (Figure 8) and appears to be a result of increased aqueous phase oxidation in that region. The region is hot and dry; as such sulfate production is predominantly gas-phase (new particles) there. However, in the future 2030 climate both H_2O_2 and cloud cover increase in that region (Figure 8), driving an increase in aqueous phase production. The H_2O_2 increases are driven by increased production rate due to enhanced OH and water vapor. Figure 8 shows the results for the B1 scenario, and a similar result is obtained for the A1B scenario. Both A1B and B1 predict substantial SO_2 emissions at 2030 along the North African coastline. CLE and MFR do not have substantial SO_2 emissions in the North African region and therefore the climate effect is less pronounced for those scenarios.

[32] Both the IPCC and IIASA scenarios suggest significant decreases in surface sulfate in the NH midlatitude region across Europe and the United States, except CLE, which has almost no change to sulfate over the United States (Figure 9). The surface sulfate decreases over Europe and the United States are about −0.5 ppbv (−50%) in A1B and −60–80% in B1. CLE predicts a −50% reduction in surface sulfate over Europe. MFR has −60–80% decreases over most of the continental Northern Hemisphere and southern Africa. A1B, CLE and B1 forecast large increases in surface sulfate over India: about 3ppbv or 200% in A1B, 100% in B1 and 150% in CLE. The A1B and B1 futures predict large increases in surface sulfate over north and east Africa and the Middle East (200% in A1B, 150% in B1). A1B has substantial increases in surface sulfate across Central and South America. The CLE future includes penetration of emissions controls on the African and South American continents and as such results in negligible changes or even decreases in surface sulfate over those regions, despite the economic development there. A1B has a significant increase in surface sulfate over China compared to a significant decrease in B1 for that region.

4.3. Changes to Global Budgets at 2030

4.3.1. Ozone

[33] The global O_3 budget is determined by three processes: net chemical production (the difference between chemical production rate and chemical loss rate), stratosphere-troposphere exchange and dry deposition. In the present simulations the stratospheric exchange term is

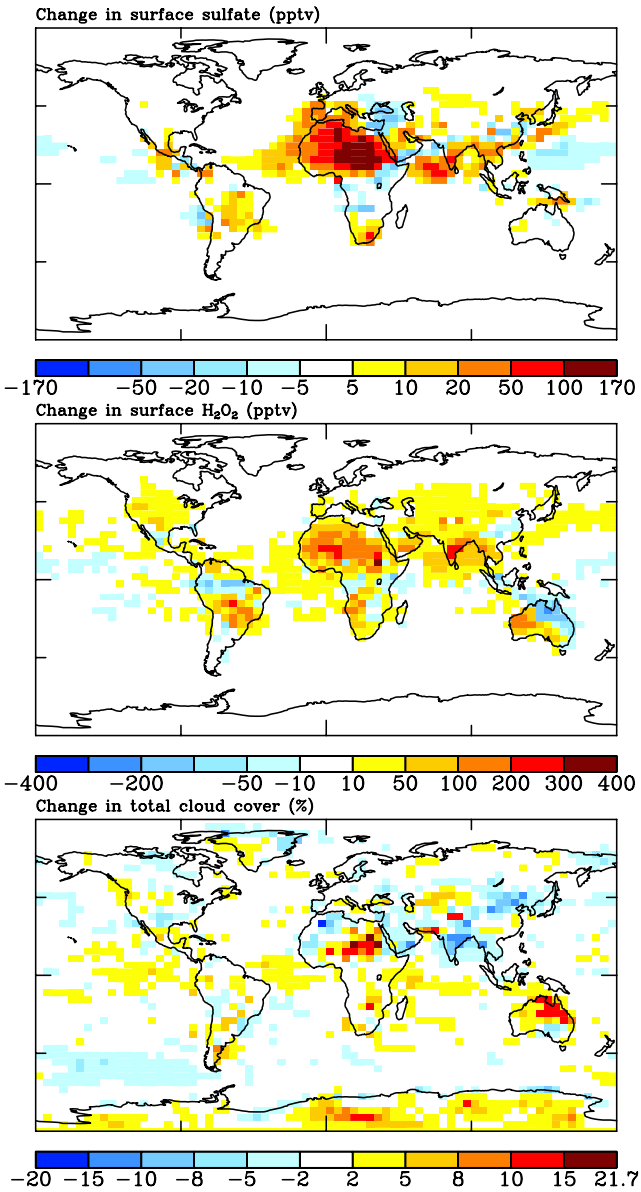

Figure 8. Impact of physical climate change on (top) surface sulfate (pptv), (middle) surface H_2O_2 (pptv), and (bottom) total cloud cover (%), at 2030 relative to the present-day calculated using the B1 scenario family.

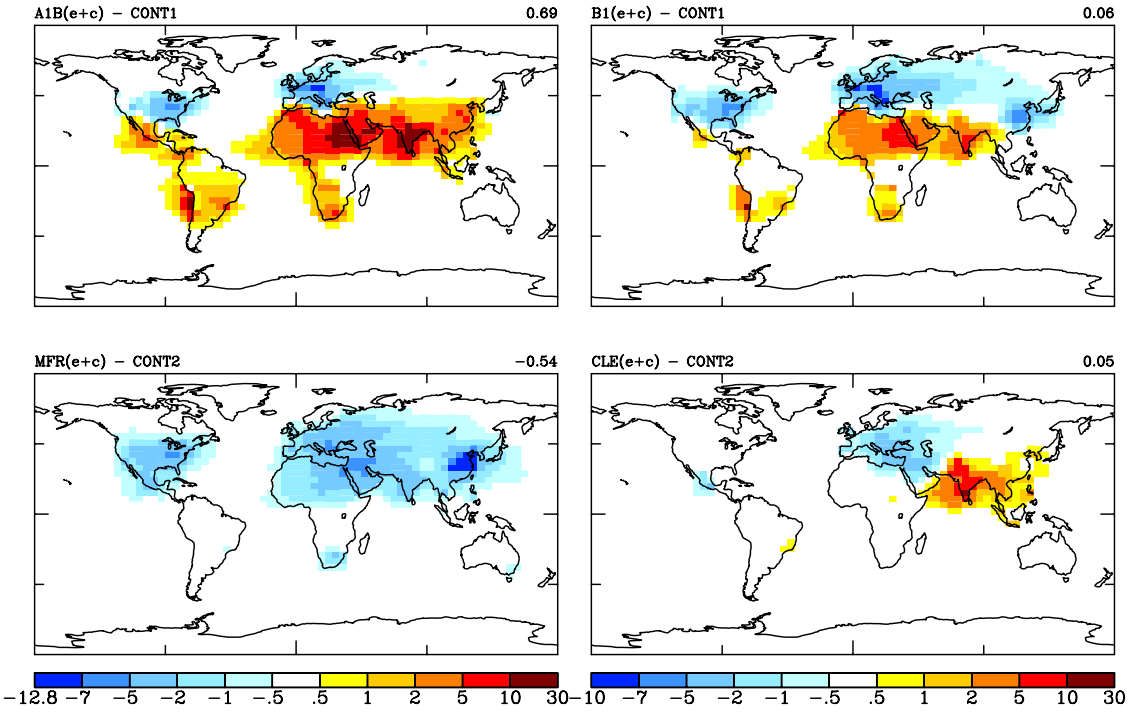

Figure 9. Total combined change (emissions and climate) in surface sulfate (10^2 pptv) for each scenario family at 2030 relative to the present-day.

inferred from a balance of the other two process terms. The A1B future would cause the largest increases in net chemical production (45%) and O_3 burden (9%) (Table 6). The B1 and CLE scenarios both forecast a modest increase in net chemical production (6–8%), which is compensated for by a small increase in dry deposition. Both scenarios suggest almost no change in the global O_3 burden despite different global NO_x emissions changes (Figure 1). MFR forecasts a −22% decrease in O_3 net chemical production, but only a −6% decrease in global O_3 burden, despite the substantial precursor emissions reductions (Figure 1). In all scenarios, physical climate changes serve to reduce the emissions-driven changes in net chemical production, dry deposition and the global O_3 burden. In the MFR scenario, the global O_3 burden is reduced by only −3% because of the emissions-only changes. The present results agree well with similar recent analyses of the 2030 O_3 budget changes [*Stevenson et al.*, 2005, 2006].

4.3.2. Sulfate

[34] The RAINS model estimates much lower SO_2 emissions over Europe than the Edgar 1995 inventory (114.6 Tg SO_2/yr for CONT2 versus 143.9 Tg SO_2/yr for CONT1, see Table 1). In the present study, we are concerned with the relative changes between each 2030 scenario and the present-day control. The A1B and MFR futures impact the global sulfate budgets dramatically (Table 7). In A1B, the global production rates of sulfate increase by about 50%, the global dry deposition increases by about 50% and wet deposition by about 40%, leading to a change in the global sulfate burden of about +43%, with no change in the lifetime. Conversely, in the MFR future, global production rates of sulfate decrease by about 35%, the global dry deposition decreases by about 45% and wet deposition by about 33%, leading to a change in the global sulfate burden of about −35%. The CLE future predicts about a 7% increase in global sulfate burden, with about a 10% increase in gas-phase and aqueous-phase production rates. The B1 future has a global decrease in SO_2 emissions (for example, Figure 1) but a small global increase in the sulfate burden (Table 7), owing to the regional shift in SO_2 emissions to more subtropical regions characterized by high aseasonal oxidation rates and low wet deposition, (in contrast to NH midlatitudes, which are characterized by seasonal oxidant limitation and high wet deposition rates). The B1 scenario demonstrates the importance of the spatial location of the emissions in determining the climate and air pollution

Table 6. Relative Roles of Emissions and Climate Changes on the Global O_3 Budget for Each Scenario[a]

	IPCC SRES			IIASA		
	CONT1	A1B	B1	CONT2	CLE	MFR
Chemistry, Tg O_3 yr^{-1}	478	692 (721)	508 (533)	547	589 (617)	428 (452)
Stratosphere, Tg O_3 yr^{-1}	634	620 (616)	632 (629)	632	623 (626)	634 (638)
Dry deposition, Tg O_3 yr^{-1}	−1112	−1311 (−1337)	−1140 −(1162)	−1180	−1212 −(1243)	−1062 −(1090)
Burden, Tg O_3	451	491 (502)	455 (465)	464	466 (479)	436 (448)

[a]The value shown in each cell is for the total combined emissions and climate change simulation (i.e., S(e+c)). The number in parentheses is for the emissions-only simulation (i.e., S(e)).

Table 7. Relative Roles of Emissions and Climate Changes on Global Sulfate Budget for Each Scenario[a]

	IPCC SRES			IIASA		
	CONT1	A1B	B1	CONT2	CLE	MFR
			Sources, Tg S yr^{-1}			
Direct emission	2.2	2.8	1.8	1.7	1.7	0.7
Gas phase	13.6	20.0 (19.7)	14.5 (14.3)	12.7	14.0 (13.9)	8.4 (8.4)
Aqueous phase	13.7	19.1 (19.1)	14.1 (14.1)	12.4	13.4 (13.5)	8.4 (8.4)
			Sinks, Tg S yr^{-1}			
Dry deposition	−3.8	−5.7 (−5.5)	−4.0 (−3.9)	−3.4	−3.6 (−3.5)	−1.9 (−1.9)
Wet deposition	−25.6	−36.1 (−36.0)	−26.3 (−26.3)	−23.3	−25.6 (−25.6)	−15.6 (−15.7)
Burden, Tg S	0.49	0.70 (0.70)	0.52 (0.53)	0.46	0.49 (0.50)	0.30 (0.30)
Lifetime, days	6.1	6.1 (6.2)	6.3 (6.4)	6.3	6.1 (6.3)	6.3 (6.2)

[a]The value shown in each cell is for the total combined emissions and climate change simulation (i.e., S(e+c)). The number in parentheses is for the emissions-only simulation (i.e., S(e)).

response. In general, the global sulfate burden change does not respond linearly to the global SO_2 emissions change (compare Tables 1 and 7). In A1B the sulfate burden increase (∼42%) is amplified relative to the SO_2 emissions increase (∼33%), while in MFR the sulfate burden decrease (∼−35%) is dampened relative to the SO_2 emissions decrease (∼−65%).

[35] Physical climate changes do not exert a large impact relative to the emissions-driven changes for sulfate, at least on global scales. The most significant climate influence on the global sulfate budget appears to be an enhancement of gas-phase sulfate production by about 3–4%, reflecting increased oxidant levels in the future climate. In addition, regional precipitation increases in the future climate (Figure 2) lead to increased wet deposition of sulfate over China and the Southern Ocean, which reduces the global burden slightly.

4.3.3. Methane

[36] Table 8 summarizes the important CH_4 budget terms for present-day simulations and future projections. A1B forecasts a large increase in global CH_4 burden by 2030 (43%). B1 also has a large increase in CH_4 burden (22%). In the CLE and MFR simulations, CH_4 concentrations were fixed to values previously generated with the STOCHEM model [*Dentener et al.*, 2004], yielding CH_4 global burden changes in our model of 14% and −4%, respectively. B1 and CLE feature similar global man-made CH_4 emissions changes (+20%), but B1 has a substantially higher CH_4 burden and surface CH_4 concentration at 2030 than CLE. The enhanced burden in B1 relative to CLE may reflect the difference in NO_x emissions changes for those scenarios, which increase in CLE but decrease in B1, an idea supported by the shortened CH_4 lifetime in CLE compared with B1. However, it is difficult to compare since in the B1 family simulations included a full calculation of CH_4 whereas in CLE, CH_4 was prescribed.

5. Radiative Forcing

[37] We use instantaneous direct radiative forcing as a tool to assess the impact of future changes in the tropospheric burdens of O_3, CH_4, and sulfate on the radiative balance of the Earth system. The adjusted forcing would provide a better indication of the climate response in the case of O_3 and this value would be slightly less [e.g., *Hansen et al.*, 1997]. The tropopause radiative forcings of O_3 and sulfate aerosol are calculated within the GISS climate model's internal radiative transfer scheme, which incorporates relative humidity dependence [*Schmidt et al.*, 2006]. Tropospheric O_3 and sulfate aerosol have extremely inhomogeneous spatial distributions, leading to similar inhomogeneity in the radiative forcings. Previous CTM studies have assumed a constant forcing per unit ozone change, thus neglecting the influence of spatial changes in the O_3 distribution [*Wild et al.*, 2001; *Fiore et al.*, 2002]. The CH_4 radiative forcing is calculated using a standard simplified expression based on concentration change, appropriate for small changes in concentration [*Ramaswamy et al.*, 2001].

[38] The global mean annual average direct radiative forcings of O_3, CH_4, and sulfate due to composition changes at 2030 relative to present-day for each future projection are presented in Table 9. For O_3 the sum of shortwave and longwave radiative forcing is given, whereas for sulfate the shortwave radiative forcing is shown. For comparison, the estimated radiative forcings between present-day and the preindustrial era are included [*Ramaswamy et al.*, 2001].

Table 8. Relative Roles of Emissions and Climate Changes on CH_4 Concentrations and Budget Terms[a]

	IPCC			IIASA		
	CONT1	A1B	B1	CONT2	CLE	MFR
Global mean surface concentration, ppbv	1729	2478 (2522)	2117 (2141)	1760	2012 (2088)	1696 (1760)
Burden, Tg	4700	6723 (6849)	5749 (5820)	4845	5539 (5748)	4669 (4845)
Chemical loss rate, Tg CH_4 yr^{-1}	−505	−714 (−698)	−628 (−611)	−528	−621 (−615)	−531 (−527)
Lifetime,[b] yrs	8.8	9.0 (9.4)	8.7 (9.1)	8.7	8.5 (8.9)	8.3 (8.7)

[a]The value shown in each cell is for the total combined emissions and climate change simulation (i.e., S(e+c)). The number in parentheses is for the emissions-only simulation (i.e., S(e)).

[b]Includes soil sink of 30 Tg CH_4 yr^{-1}.

Table 9. O_3, CH_4, and Sulfate Radiative Forcing in Units of mW m^{-2} at 2030 Relative to Present-Day for Each Scenario Due to Emissions Only and Emissions and Climate Changes[a]

Scenario Family	Global Change	O_3	Sulfate	CH_4	Total
PI to PD		350.0	−400.0	480.0	430.0
A1B	emissions-only	190.0	−240.0	264.1	214.1
A1B	total	140.0	−220.0	250.1	170.1
B1	emissions-only	50.0	−30.0	143.7	163.7
B1	total	20.0	−10.0	135.2	145.2
CLE	emissions-only	59.4	−43.7	115.7	131.4
CLE	total	12.3	−38.0	89.8	64.1
MFR	emissions-only	−51.9	174.0	0.0	122.1
MFR	total	−96.6	178.3	−23.8	57.9

[a]The pre-industrial to present-day change (PI to PD) is indicated for comparison.

[39] The resultant forcings span a wide range across the scenarios: +260 to −20.0 mW/m^2 for CH_4, +190 to −97 mW/m^2 for O_3, and −240.0 to +180.0 mW/m^2 for sulfate aerosol. The A1B, B1, and CLE projections all show positive forcing for CH_4 and O_3 and negative forcing for sulfate aerosol between 2030 and the present-day. A1B features the largest absolute forcings, each component exerts a forcing approximately half that of the PI to PD change. In contrast, in the MFR scenario, the signs of the forcings for each component are reversed; that is, negative forcing for O_3 and CH_4 and positive forcing for sulfate aerosol. The reversal in sulfate forcing in the MFR scenario leads to an overall positive forcing for this scenario, despite negative forcings from O_3 and CH_4. Previous studies examining the climate impacts of the MFR scenario have considered only O_3 and CH_4 [*Dentener et al.*, 2004; *Stevenson et al.*, 2005]. Our studies reveal that including the impact of sulfate changes presents a significantly different picture with important implications for future climate change under the MFR scenario.

[40] Results from a recent multimodel ensemble investigation, in which the present model was a participant, using the CLE and MFR scenarios indicate combined CH_4 and O_3 forcings of +180 mW/m^2 (CLE) and −40 mW/m^2 (MFR) [*Stevenson et al.*, 2006]. The O_3 forcings in the present study compare well with the mean values from the multi model study. For CLE emissions only, the present study O_3 forcing is +59 mW/m^2 versus 63 ± 16 mW/m^2 in the multimodel study. For MFR emissions only, the present study O_3 forcing is −52 mW/m^2 versus −43 ± 15 mW/m^2 in the multimodel study. However, inclusion of the sulfate and CH_4 forcings in our study, leads to similar combined forcings for CLE and MFR (∼+60 mW/m^2).

[41] The coupling of climate change effects to the emissions changes reduces the absolute magnitude of the forcing for all three components. In general, the impact of climate change on the CH_4 forcing is small (about 5% for the IPCC scenarios, up to 20% for the IIASA scenarios which used prescribed CH_4 concentrations). The O_3 and sulfate forcings are more sensitive to the inclusion of climate change effects. For the B1 and CLE scenarios, inclusion of the tropospheric response to climate change dampens the O_3 forcing by 60–80%. Hence impacts of climate changes are comparable to emissions changes for the CLE and B1 scenarios.

6. Conclusions

[42] We have applied the GISS composition-climate model to explore changes to O_3, CH_4, and sulfate aerosol at 2030 on the basis of four different future scenarios of man-made emissions. The A1B, B1, and CLE futures all suggest a spreading of global air pollution to lower subtropical and tropical latitudes as more nations industrialize. Existing air pollution at northern midlatitudes either increases (A1B), decreases (B1), or remains approximately the same (CLE). The range of regional average surface O_3 changes spans −10 to +30 ppbv and the range of regional average surface sulfate changes spans −1200 to 3000 pptv dependent on the scenario. There is a temporal persistence of the surface O_3 air pollution in subtropics versus midlatitudes. The Indian subcontinent appears to be a future hot spot for O_3 and sulfate pollution because of the large man-made emissions increases projected in the A1B, B1, and CLE scenarios.

[43] We have found a range of projected radiative forcings dependent on the scenario: CH_4 (260 to −20 mWm^{-2}), O_3 (+190 to −10 mWm^{-2}), sulfate (−240 to +180 mWm^{-2}). The forcings may be as much as half that of the preindustrial to present-day forcing (A1B). All the scenarios have a combined positive forcing, which in the case of the MFR scenario is due to a relatively large positive forcing from the reduced sulfate burden.

[44] In general, physical climate changes dampen climate and air pollution effects of increased man-made emissions, although do increase surface sulfate. For the CLE and B1 scenarios the impacts of physical climate changes on O_3 and sulfate are of comparable magnitude to the emissions changes whereas A1B and MFR responses are dominated by the man-made emissions changes. Climate change reduced the radiative forcings, 5–20% for CH_4 and up to 60–80% for O_3 and sulfate (B1 and CLE).

[45] Despite aggressive (expensive) reductions in O_3 precursor gases, the dramatic reductions in sulfate in the MFR future lead to an overall combined positive radiative forcing of similar magnitude to the CLE future. The positive forcing from sulfate reduction will have to be faced at some point, after 2030 if not before. Analysis over a longer time horizon would put the MFR scenario in a more favorable light relative to the other projections. The B1 future enjoys reductions in surface O_3 and sulfate across the world's most polluted regions relative to the present-day, but results in a larger CH_4 forcing (and therefore overall combined forcing) than the CLE future, which has similar or slightly larger surface O_3 values by 2030 relative to the present-day in the NH polluted midlatitude belt. For the A1B future, man strongly negatively influences the quality of the environment through emissions-driven changes in O_3, sulfate and CH_4. In particular, global increases in CH_4 emissions in A1B drive regional increases in surface O_3 pollution in areas, especially the eastern United States, where other precursor emissions (NO_x, CO) have decreased. However, the climate change scenario that we employ represents about 3/4 of the climate change from the A1B scenario. Use of the consistent A1B climate change scenario would

most likely lead to lower surface O_3, higher surface sulfate and lower CH_4 concentrations than in the present study, although the man-made emissions changes would still dominate the overall changes for this scenario.

[46] The current study has some limitations. We do not consider the impacts of physical climate changes (for example, temperature, humidity, and precipitation) on important biogenic trace gas emissions including isoprene (a major natural O_3 precursor), other NMVOCs from vegetation and NO_x from soils. Furthermore, the vegetation distribution itself will change in the future because of climate changes and man-made activities such as deforestation, which will influence trace gas emissions and deposition. Neither do we consider future changes in stratospheric composition in the present study. Therefore changes in stratosphere-troposphere exchange are not fully treated. Heterogeneous reactions on mineral dust and interactions with other aerosol types (for example, carbonaceous and nitrate) have not been included in this study although other work suggests sizable forcings, which may impact the present results [e.g., *Hansen*, 2002, and references therein]. Our future modeling efforts will move us toward more realistic models incorporating these aforementioned processes, including interactive biogenic emissions, dynamic vegetation, stratospheric chemistry and heterogeneous aerosol-chemistry interactions. Nevertheless, the present results do provide effective limits for the magnitude of possible future changes to O_3, sulfate and CH_4 composition at 2030. We intend to investigate other relevant future time frames (for example, 2050 and 2100) and examine the influence of particular emission sectors (for example, biomass burning versus fossil fuel burning) on future air quality and radiative forcing.

[47] **Acknowledgments.** This research was supported by the NASA Atmospheric Chemistry Modeling and Analysis Program (ACMAP). We thank the NASA Center for Computational Sciences for computing support.

References

Amann, M., I. Bertok, J. Cofola, F. Gyarfas, C. Heyes, Z. Kilmont, M. Makowski, W. Schopp, and S. Syri (1999), Cost-effective control of acidification and ground level ozone, seventh interim report, Int. Inst. for Appl. Syst. Anal., Laxenburg, Austria.

Baughcum, S. L., T. G. Tritz, S. C. Henderson, and D. C. Pickett (1996), *Scheduled Civil Aircraft Emission Inventories for 1992: Database Development and Analysis*, *NASA-CR-4700*, 205 pp., Natl. Aeronaut. and Space Admin., Langley Res. Cent., Hampton, Va.

Bell, N., D. Koch, and D. T. Shindell (2005), Impacts of chemistry-aerosol coupling on tropospheric ozone and sulfate simulations in a general circulation model, *J. Geophys. Res.*, *110*, D14305, doi:10.1029/2004JD005538.

Berglen, T. F., T. K. Berntsen, I. S. A. Isaksen, and J. K. Sundet (2004), A global model of the coupled sulfur/oxidant chemistry in the troposphere: The sulfur cycle, *J. Geophys. Res.*, *109*, D19310, doi:10.1029/2003JD003948.

Berntsen, T., J. S. Fuglestvedt, M. Joshi, K. P. Shine, N. Stuber, R. Sausen, L. Li, D. A. Hauglustaine, and M. Ponater (2005), Climate response to regional emissions of ozone precursors: Sensitivities and warming potentials, *Tellus, Ser. B*, *57*, 283–304.

Dentener, F., D. Stevenson, J. Cofala, R. Mechler, M. Amann, P. Bergamaschi, F. Raes, and R. Derwent (2004), The impact of air pollutant and methane emission controls on tropospheric ozone and radiative forcing: CTM calculations for the period 1990–2030, *Atmos. Chem. Phys. Discuss.*, *4*, 1–68.

Dentener, F., et al. (2006), The global atmospheric environment for the next generation, *Environ. Sci. Technol.*, *40*, 3586–3594

Emberson, L. D., , M. R. Ashmore, F. Murray (Eds.) (2003), *Air Pollution Impacts on Crops and Forests: A Global Perspective*, Imperial Coll. Press, London.

Feichter, J., E. Roeckner, U. Lohmann, and B. Liepert (2004), Nonlinear aspects of the climate response to greenhouse gas and aerosol forcing, *J. Clim.*, *17*, 2384–2398.

Fiore, A. M., D. J. Jacob, B. D. Field, D. G. Streets, S. D. Fernandes, and C. Jang (2002), Linking ozone pollution and climate change: The case for controlling methane, *Geophys. Res. Lett.*, *29*(19), 1919, doi:10.1029/2002GL015601.

Fuglestvedt, J. S., T. Berntsen, I. S. A. Isaksen, H. Mao, X.-Z. Liang, and W.-C. Wang (1999), Climatic forcing of nitrogen oxides through changes in tropospheric ozone and methane: Global 3D model studies, *Atmos. Environ.*, *33*, 961–977.

Fuglestvedt, J. S., T. Berntsen, O. Godal, R. Sausen, K. P. Shine, and T. Skodvin (2003), Metrics of climate change: Assessing radiative forcing and emission indices, *Clim. Change*, *58*, 267–331.

Guenther, A. B., et al. (1995), A global model of natural volatile organic compound emissions, *J. Geophys. Res.*, *100*, 8873–8892.

Hansen, J. E. (2002), *Air Pollution as a Climate Forcing*, 169 pp., NASA Goddard Inst. for Space Stud., New York.

Hansen, J., M. Sato, and R. Ruedy (1997), Radiative forcing and climate response, *J. Geophys. Res.*, *102*, 6831–6864.

Hansen, J., M. Sato, R. Ruedy, A. Lacis, and V. Oinas (2000), Global warming in the twenty-first century: An alternative scenario, *Proc. Natl. Acad. Sci. U. S. A.*, *97*, 9875–9880.

Hansen, J., and M. Sato (2004), Greenhouse gas growth rates, *Proc. Natl. Acad. Sci. U. S. A.*, *101*, 16,109–16,114.

Hein, R., P. J. Crutzen, and M. Heimann (1997), An inverse modeling approach to investigate the global atmospheric methane cycle, *Global Biogeochem. Cycles*, *11*, 43–76.

Henderson, S. C., and U. K. Wickrama (1999), Aircraft emissions: Current inventories and future scenarios, in *Aviation and the Global Atmosphere*, edited by J. E. Penner et al., pp. 291–332, Cambridge Univ. Press, New York.

Houweling, S., T. Kaminski, F. Dentener, J. Lelieveld, and M. Heimann (1999), Inverse modeling of methane sources and sinks using the adjoint of a global transport model, *J. Geophys. Res.*, *104*, 26,137–26,160.

IMAGE Team (2001), *The Image 2. 2 Implementation of the SRES Scenarios*, *CD-ROM Publ. 481508018*, Natl. Inst. for Public Health and the Environ., Bilthoven, The Netherlands.

Intergovernmental Panel on Climate Change (2001), *Climate Change 2001: The Scientific Basis*, edited by J. T. Houghton et al., 881 pp., Cambridge Univ. Press, New York.

Johnson, C. E., D. S. Stevenson, W. J. Collins, and R. G. Derwent (2001), Role of climate feedback on methane and ozone studied with a coupled ocean-atmosphere-chemistry model, *Geophys. Res. Lett.*, *28*, 1723–1726.

Koch, D., D. Jacob, I. Tegen, D. Rind, and M. Chin (1999), Tropospheric sulfur simulation and sulfate direct radiative forcing in the Goddard Institute for Space Studies general circulation model, *J. Geophys. Res.*, *104*, 23,799–23,822.

Koch, D., G. A. Schmidt, and C. V. Field (2006), Sulfur, sea salt, and radionuclide aerosols in GISS ModelE, *J. Geophys. Res.*, *111*, D06206, doi:10.1029/2004JD005550.

Lucarini, V., and G. L. Russell (2002), Comparison of mean climate trends in the Northern Hemisphere between National Centers for Environmental Prediction and two atmosphere-ocean model forced runs, *J. Geophys. Res.*, *107*(D15), 4269, doi:10.1029/2001JD001247.

Matthews, E. (2000), Wetlands, in *Atmospheric Methane: Its Role in the Global Environment*, edited by M. A. K. Khalil, pp. 202–233, Springer, New York.

Naik, V., D. Mauzerall, L. Horowitz, M. D. Schwarzkopf, V. Ramaswamy, and M. Oppenheimer (2005), Net radiative forcing due to changes in regional emissions of tropospheric ozone precursors, *J. Geophys. Res.*, *110*, D24306, doi:10.1029/2005JD005908.

Nakicenovic, N., et al. (2000), *Special Report on Emission Scenarios*, 559 pp., Cambridge Univ. Press, New York.

Olivier, J. G. J., and J. J. M. Berdowski (2001), Global emissions sources and sinks, in *The Climate System*, edited by J. Berdowski, R. Guicherit, and B. J. Heij, pp. 33–78, A. A. Balkema, Brookfield, Vt.

Park, R. J., D. J. Jacob, B. D. Field, R. M. Yantosca, and M. Chin (2004), Natural and transboundary pollution influences on sulfate-nitrate-ammonium aerosols in the United States: Implications for policy, *J. Geophys. Res.*, *109*, D15204, doi:10.1029/2003JD004473.

Penner, J. E., et al. (2001), Aerosols: Their direct and indirect effects, in *Climate Change 2001: The Scientific Basis*, edited by J. T. Houghton et al., chap. 5, pp. 289–348, Cambridge Univ. Press, New York.

Pope, C. A., III (2004), Air pollution and health: Good news and bad, *N. Engl. J. Med.*, *351*(11), 1132–1134.

Prather, M., and D. Ehhalt (2001), Atmospheric chemistry and greenhouse gases, in *Climate Change 2001: The Scientific Basis*, edited by J. T.

Houghton et al., chap. 4, pp. 239–287, Cambridge Univ. Press, New York.

Price, C., J. Penner, and M. Prather (1997), NO_x from lightning: 1. Global distribution based on lightning physics, *J. Geophys. Res.*, *102*, 5929–5941.

Ramaswamy, V., et al. (2001), Radiative forcing of climate change, in *Climate Change 2001: The Scientific Basis*, edited by J. T. Houghton et al., pp. 349–416, Cambridge Univ. Press, New York.

Russell, G. L., J. R. Miller, D. Rind, R. A. Ruedy, G. A. Schmidt, and S. Sheth (2000), Comparison of model and observed regional temperature changes during the past 40 years, *J. Geophys. Res.*, *105*, 14,891–14,898.

Rypdal, K., T. Berntsen, J. S. Fuglestvedt, K. Aunan, A. Torvanger, F. Stordal, J. M. Pacyna, and L. P. Nygaard (2005), Tropospheric ozone and aerosols in climate agreements: Scientific and political challenges, *Environ. Sci. Policy*, *8*, 29–43.

Schmidt, G. A., et al. (2006), Present day atmospheric simulations using GISS ModelE: Comparison to in-situ, satellite and reanalysis data, *J. Clim.*, *19*, 153–192.

Shindell, D. T., G. Faluvegi, and N. Bell (2003), Preindustrial-to-present-day radiative forcing by tropospheric ozone from improved simulations with the GISS chemistry-climate GCM, *Atmos. Chem. Phys.*, *3*, 1675–1702.

Shindell, D. T., B. P. Walter, and G. Faluvegi (2004), Impacts of climate change on methane emissions from wetlands, *Geophys. Res. Lett.*, *31*, L21202, doi:10.1029/2004GL021009.

Shindell, D. T., G. Faluvegi, N. Bell, and G. A. Schmidt (2005), An emissions-based view of climate forcing by methane and tropospheric ozone, *Geophys. Res. Lett.*, *32*, L04803, doi:10.1029/2004GL021900.

Stevenson, D. S., C. E. Johnson, W. J. Collins, R. G. Derwent, and J. M. Edwards (2000), Future estimates of tropospheric ozone radiative forcing and methane turnover: The impact of climate change, *Geophys. Res. Lett.*, *27*, 2073–2076.

Stevenson, D., R. Doherty, M. Sanderson, C. Johnson, B. Collins, and D. Derwent (2005), Impacts of climate change and variability on tropospheric ozone and its precursors, *Faraday Disc.*, *130*, 1–17.

Stevenson, D. S., et al. (2006), Multimodel ensemble simulations of present-day and near-future tropospheric ozone, *J. Geophys. Res.*, *111*, D08301, doi:10.1029/2005JD006338.

Streets, D. G., T. C. Bond, T. Lee, and C. Jang (2004), On the future of carbonaceous aerosol emissions, *J. Geophys. Res.*, *109*, D24212, doi:10.1029/2004JD004902.

West, J. J., and A. M. Fiore (2005), Management of tropospheric ozone by reducing methane emissions, *Environ. Sci. Technol.*, *39*(13), 4685–4691, doi:10.1021/es048629f.

Wild, O., and H. Akimoto (2001), Intercontinental transport of ozone and its precursors in a three-dimensional global CTM, *J. Geophys. Res.*, *106*, 27,729–27,744.

Wild, O., M. J. Prather, and H. Akimoto (2001), Indirect long-term global cooling from NO_x emissions, *Geophys. Res. Lett.*, *28*, 1719–1722.

M. Amann and J. Cofala, International Institute for Applied Systems Analysis, A-2361 Laxenburg, Austria.

D. M. Koch, D. T. Shindell, and N. Unger, NASA Goddard Institute for Space Studies, Columbia University, 2880 Broadway, Suite 660, New York, NY 10025, USA. (nunger@giss.nasa.gov)

D. G. Streets, Argonne National Laboratory, 9700 S. Cass Avenue, Argonne, IL 60439, USA.